2

Digital Holography: Computer-Generated Holograms and Diffractive Optics in Scalar Diffraction Domain

Giuseppe A. Cirino[1], Patrick Verdonck[2], Ronaldo D. Mansano[3], José C. Pizolato Jr.[1], Daniel B. Mazulquim[4] and Luiz G. Neto[4]
[1]*CCET - Universidade Federal de São Carlos,*
[2]*IMEC,*
[3]*EPUSP – Universidade de São Paulo,*
[4]*EESC - Universidade de São Paulo,*
[1,3,4]*Brasil*
[2]*Belgium*

1. Introduction

The invention of holography by D. Gabor, followed by the works of E. Leith and Upatnieks, made possible to perform nearly arbitrarily wavefront transformations with the aid of optical microstructures fabricated by interference (Gabor, 1948; Leith & Upatnieks, 1962; Denisyuk, 1962; Benton, 1969). The realization by A. Lohmann and co-workers in the mid-1960's that optical holograms can be simulated by digitally generated binary transparencies was another significant step forward in the path towards widespread application of diffraction in optics (Lohmann, 1956; Brown & Lohmann 1966; Lohmann & Paris, 1967). This new approach was called digital holography, or equivalently computer-generated holography. The computer-generated hologram (CGH) is distinguished primarily from its optical cousin by the fact that the computer is able to design a hologram of a non-existent, synthetic or virtual object, and the operation of the diffractive optical element (DOE) can be optimized mathematically rather than experimentally (Turunen & Wyrowski, 1997). This is clear from the words of Professor Lohmann himself, commenting on the shift from classic holography to digital holography (Lohmann, 2008):

> "we considered images as information, and we applied notions about carriers from communications and information theory [...]. In other words, our approach represented a paradigm shift from physical optics to optical information processing. "

Since the operation of CGH is based on the diffraction of light, this field is also called diffractive optics. Its essence is the control of optical fields by microstructured media (Turunen & Wyrowski, 1997).

The DOE is an optical device whose superficial microrelief has a height comparable to the light wavelength used. The DOE may be implemented in the form of a transparency or a reflecting mirror.

Throughout this text the terms computer-generated holograms (CGH), diffractive optical element (DOE), or simply hologram are employed with no distinction among each other.

The goal of digital holography is to form a light distribution in the observation (or reconstruction) plane. There are many successful applications in advanced scientific and technological fields, such as optical lithography and fabrication, and photonic manipulation of particles (optical tweezers). Lenses, zone plates, diffraction gratings, array illuminators, kinoforms, and the phase spatial filters are other examples of DOEs (Soifer et al., 1997).
The technology of DOE manufacturing involves microfabrication processes which have been maturated from microelectronics and MEMS/MOEMS technologies. Once the design is completed, an accurate process is used to materialize the DOE, such as laser, electron or ion beam writing, half-tone mask technique, diamond turning, and so on. A broad list of micromachining approaches is described in references (Herzig 1997; Turunen & Wyrowski, 1997). For a low-cost, mass production, of surface-relief microstructures, replication techniques must be used. It includes technologies such as hot embossing, casting and injection molding (Herzig 1997; Turunen & Wyrowski, 1997).
This chapter covers some aspects of design and fabrication of CGHs, operating in the scalar diffraction domain, implemented in a multi-level surface-microrelief. The specific contributions of the presented research, is the implementation of a full complex-amplitude modulation CGH, sections 3.2-3.5. Its design is based in a sub-cell approach, which increases the degree of freedom, enabling high quality diffraction patterns. Another contribution - in the fabrication of such a diffractive element - is the employment of an amorphous hydrogenated carbon (a:C-H) thin film, also known as Diamond-Like Carbon (DLC). A patented reactive magnetron sputtering technique used to produce the DLC thin film, proved to be very suitable for diffractive optics applications. Examples of amplitude-only, phase-only and complex amplitude modulation CGHs, operating in both Fraunhofer and Fresnel regimes, are presented (Neto et al, 2001, 2003, 2004, 2008).

2. Design of computer-generated holograms

The design of CGHs can be divided into three basic stages (Mait, 1995): (1) understand the physics of the design problem (analysis), (2) translate the physical understanding into mathematics and define an appropriate optimization problem (synthesis), and (3) execute the design and fabricate the element (implementation).
In the second stage one has to decide if scalar diffraction is enough to solve the problem accuratelly or it demands rigorous analytic solutions based on vectorial electromagnetic theory. Generally, rigorous analytical solution is difficult to obtain and tend to be computationally time-consuming (Turunen & Wyrowski, 1997). For most applications the employment of scalar diffraction theory is enough to represent practical engineering solutions (Mait, 1995). The analysis of DOEs by the employment of rigorous vector diffraction theory is beyond the scope of this chapter.
A DOE is designed using computer calculations based on the scalar diffraction of light, on the characteristics of the material (media) where DOE is to be fabricated, on the desired light distribution to be generated and determined by the fact of generating a phase-only or an amplitude-only distribution (object). To assure scalar domain, a linear dimension that reflects the smallest feature of the microrelief, D_{min}, must be at least ten times larger than the operating wavelength, λ. In the examples shown in section 3, the minimum feature size is $10X10\ \mu m$, and the diffractive elements operate at $632.8\ nm$ wavelength He-Ne laser. Therefore the inequality above holds: $(10/0.633) = 15.8$.
Light, considered in terms of the scalar diffraction theory, being monochromatic and coherent, is described by a complex function of two spatial variables. The propagation of

light in free space can be described using the Kirchhoff diffraction approximation, and the mathematical aspect of light propagation through an optical element reduces to the multiplication of the complex function of incident light by the complex transmittance of the optical element (Soifer et al., 1997).

Calculate a CGH means the calculation of its complex transmittance. This transmittance is expressed as $g(x',y') = A(x',y').exp[j\varphi(x',y')]$, where $A(x',y')$ is its amplitude distribution, $\varphi(x',y')$ is its phase distribution, and (x',y') are coordinates in the frequency space.

The phase modulation can be obtained by a microstructured surface of an optical medium. Amplitude modulation can be obtained by selectivelly blocking/attenuating the light intensity along the device's surface.

Depending on the media where the DOE is to be fabricated, one can refer to

i. phase-only DOE: When such a media is able to modulate only the phase of an incoming wavefront, the transmittance amplitude being equals unity;
ii. amplitude-only DOE: When such a media is able to modulate only the amplitude of an incoming wavefront, the transmittance phase being equals to a constant, or
iii. complex-amplitude DOE: When such a media is able to modulate both the phase and amplitude of an incoming wavefront.

To generate the reconstruction, it is possible to choose between designing a Fourier DOE, which employs Fraunhofer diffraction for the calculation of the element and a Fourier lens to implement the optical reconstruction, as shown in figure 1a, or a Fresnel DOE, by considering only the free space propagation of the light to generate the optical reconstruction, as shown in figure 1b.

If the element is illuminated by a uniform monochromatic coherent plane wave with a constant spatial amplitude distribution equals to *1*, the light distribution just after the element has the form $1 \times g(x',y') = g(x',y')$. The light propagation of the distribution $g(x',y')$ results in the optical distribution $g(x,y)$, located in the reconstruction plane, figure 1.

In the calculation of a DOE, the following design issues must be considered:

- Determination of the light wavefront modulation distribution $g(x',y')$ that should be generated in the DOE plane. The calculation of this distribution starts from the inverse light propagation of the desired light distribution $f(x,y)$ that should be generated in the reconstruction plane, back to the DOE plane. The main goal in the design is to determine the DOE distribution $g(x',y')$ that generates a reconstruction $g(x,y)$ as close as possible to the desired distribution $f(x,y)$, with $0 \leq |f(x,y)| \leq 1$. This light distribution $f(x,y)$ should be described in such a way as to permit computational manipulation, generally in a discrete form (usually discrete values of amplitude).
- The resulting inverse light propagation distribution f(x',y') usually presents values of both phase and amplitude, which means that this distribution must be adapted to the possible DOE distribution g(x',y'), which can be a phase-only, an amplitude-only or a complex-amplitude distribution. The physical and practical limitations of the DOE medium will determine the choice of the numerical method used for its implementation.
- A distinction is made between complex amplitude objects and intensity objects (only amplitude determined). In this manner, for complex amplitude objects one has: $f(x,y) = |f(x,y)|\exp[\varphi(x,y)]$, and for intensity $i(x,y)$ objects: $|f(x,y)|^2 = i(x,y)$, where the argument value $\varphi(x,y)$ of $f(x,y)$ has total freedom and could assume any value, hence: $f(x,y) = \sqrt{i(x,y)}\exp\left[i\varphi(x,y)\right]$.

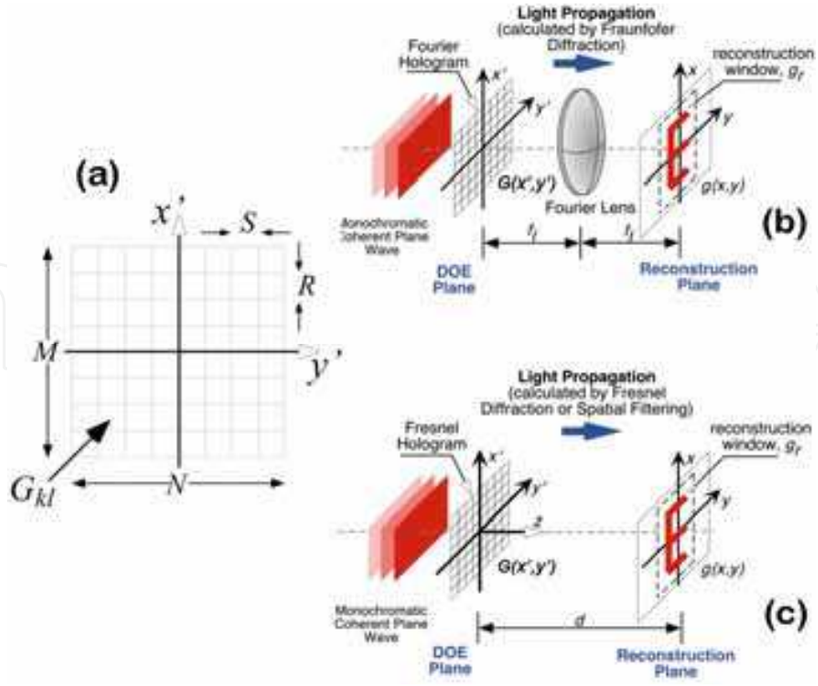

Fig. 1. (a) Hologram structure; (b) Optical reconstruction of Fourier-type CGH illuminated; (c) Reconstruction of a Fresnel-type CGH, obtained by the free space light propagation of $g(x',y')$ along distance d. Reprinted with permission of SPIE (Neto, L.G. 2004).

The hologram is considered a two-dimensional matrix structure with M by N (M and M being even numbers) with rectangular cells of dimension R by S. Each cell represents a complex transmittance value G_{kl}. Supposing the hologram is placed in the frequency plane:

$$G(x',y') = rect\left[\frac{x'}{MR},\frac{y'}{NS}\right]\left\{\sum_{k=-M/2}^{+(M/2)-1}\sum_{l=-N/2}^{+(N/2)-1} G_{kl}\times rect\left[\frac{x'-kR}{R},\frac{y'-lS}{S}\right]\right\} \quad (1)$$

Calculating the inverse Fourier transform of equation 1, one obtains the light distribution in the image formation plane:

$$g(x,y) = M^2RS\ \mathrm{sinc}\left[MRx,NSy\right]\ \otimes \left\{\sum_{k=-M/2}^{+(M/2)-1}\sum_{l=-N/2}^{+(N/2)-1} G_{kl}\exp\left[j2\pi\left(Rxk+Syl\right)\right]\times \mathrm{RS\ sinc}\left[Rx,Sy\right]\right\} \quad (2)$$

where ⊗ denotes the convolution operation. The signal $f(x,y)$ is also represented by discrete values: $f(x,y)\leftrightarrow f_{mn}(x,y)$.
Sampling the function $g(x,y)$ with intervals X in the x direction [$x=mX=m/(MR)$] and Y in the y direction [$y=nY=n/(NS)$], one obtain (Goodman, 1996)

$$g(x,y) = \mathrm{sinc}\left[MRx,NSy\right]\ \otimes\left\{g_{mn}\sqrt{\frac{\mathrm{RS}}{\mathrm{XY}}}\ \mathrm{sinc}\left[\frac{m}{M},\frac{n}{N}\right]\right\} \quad (3)$$

where g_{mn} is the discrete inverse Fourier transform of G_{kl}:

$$g_{mn} = \frac{1}{\sqrt{MN}} \left\{ \sum_{k=-M/2}^{+(M/2)-1} \sum_{l=-N/2}^{+(N/2)-1} G_{kl} \exp \left[j2\pi \left(\frac{mk}{M} + \frac{nl}{N} \right) \right] \right\} \quad (4)$$

The discrete Fourier transform g_{mn} is obtained numerically by using the Fast Fourier Transform Algorithm (FFT) realized by (Cooley & Tukey, 1965).

2.1 Iterative Fourier Transform Algorithm (IFTA)

The FFT algorithm gives a computational basis for virtually all of iterative methods (Soifer et al., 1997). In many cases, an error reducing algorithm called Iterative Fourier Transform Algorithm (IFTA), depicted in figure 2, is a natural choice (Wyrowski, 1989, 1990).

In the IFTA, one iteration is achieved by firstly calculating the inverse light propagation from the reconstruction plane to the hologram plane, where the hologram restrictions are applied (to force a phase-only distribution, as exemplified in figure 2), and then calculating the forward light propagation from the hologram plane to the reconstruction plane, where restrictions are applied (forcing the desired intensity reconstruction $i(x,y)$). For intensity objects, a random phase distribution is attributed to $\varphi(x,y)$ in the first iteration to help in the convergence of the algorithm.

Usually these numerical methods are computer time consuming and they introduce speckle noise in the reconstruction plane. A hundred or more iterations are needed, depending on the complexity of the design and on the desired light distribution $f(x,y)$ in the CGH reconstruction plane.

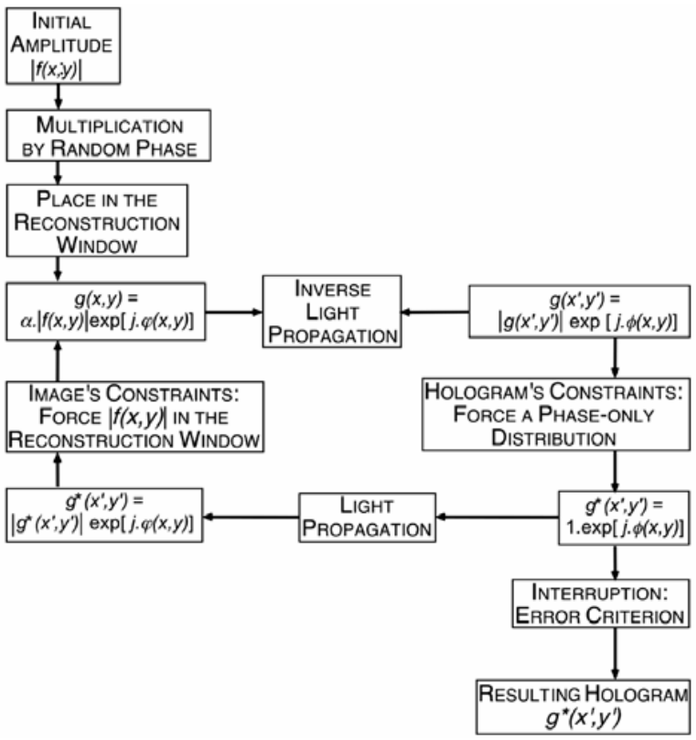

Fig. 2. Schematic flow chart illustrating the IFTA for a phase-only hologram and for intensity objects. Reprinted with permission of SPIE (Neto, L.G. 2004).

2.2 Phase, amplitude and scale freedoms

To help the convergence of the numerical method, some additional degrees of freedom can be introduced in the design. Assuming, for example, a phase-only CGH is to be designed (figure 2), they can be formulated as follows:

- Phase and amplitude freedom outside the reconstruction window g_r: outside the finite region $A \times B$ in the reconstruction plane, called reconstruction window, g_r, the phase and amplitude values for $g(x,y)$ can vary freely. The coding process of a phase-only CGH consists of finding a distribution $g(x',y')$ that satisfies the hologram modulation restrictions and ensures that the desired object $f(x,y)$ is contained within g_r , figure 3.
- Phase freedom inside g_r: for intensity objects, the phase $\varphi(x,y)$ can vary freely inside the region gr.
- Freedom of the scale factor α: One can vary the scale factor α in order to obtain an error reduction inside the region g_r , figure 2.

Assuming now a full complex-amplitude modulation CGH, there is much more flexibility in the design, considering there is always at least one solution to the problem. The complex values of transmittance of each hologram's element are directly represented by the CGH distribution $g(x',y')$, with no iterative procedures. Using this approach, the total computer time can be reduced by two orders of magnitude (Neto, et al., 2003, 2004), and the quality of reconstructed images are quite better than a phase-only CGH, as can be see in section 3.3.

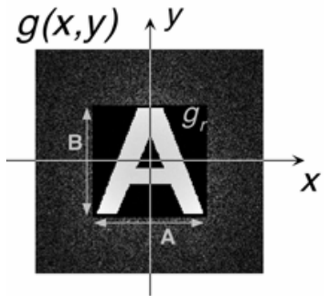

Fig. 3. Reconstruction window used to improve the DOE reconstruction. Outside the region g_r of dimensions AXB, the phase and amplitude values for $g(x,y)$ can vary freely. Reprinted with permission of SPIE (Neto, L.G. 2004).

2.3 Diffraction efficiency

The quality of the CGH calculation is evaluated via the degree of deviation of the produced image from the desired one, and via the fraction energy going onto the generation of the image. Each application has specific demands for emphasizing one or another figure of merit. The main three parameters are used (Soifer, et al., 1997):

Diffraction efficiency, η: Is the ratio of the light energy having come into a predefined area (region g_r) to the entire energy striking the DOE:

$$\eta = \frac{\sum_{m=-A/2}^{+(A/2)-1} \sum_{n=-B/2}^{+(B/2)-1} \left| g_{m-Mo,\ n-No} \right|^2}{MN} \tag{5}$$

where MN denotes the extension of the hologram when illuminated by a light wave with a constant amplitude equal to unity. It is also helpful to describe η as the product of the

transmitted, η_T, and diffracted, η_D, terms: $\eta = \eta_D \eta_T$. The term η_T gives the fraction of the energy transmitted through the hologram and the term η_D gives the fraction of the transmitted energy that forms the signal:

$$\eta_D = \frac{\sum_{m=-A/2}^{+(A/2)-1} \sum_{n=-B/2}^{+(B/2)-1} \left| g_{m-Mo,\ n-No} \right|^2}{\sum_{m=-A/2}^{+(A/2)-1} \sum_{n=-B/2}^{+(B/2)-1} \left| g_{m,n} \right|^2} \tag{6}$$

and

$$\eta_T = \frac{\sum_{m=-A/2}^{+(A/2)-1} \sum_{n=-B/2}^{+(B/2)-1} \left| G_{k,l} \right|^2}{MN} \tag{7}$$

where M_0 and N_0 are the center coordinates of the reconstruction window g_r.

For phase-only holograms, where $mod\{G_{mn}\}=1$, one has η_D=1, i.e., all energy is transmitted to form the signal and $\eta=\eta_D$. Under certain circumstances it is possible to achieve diffraction efficiencies near unity.

Considering amplitude-only holograms, it is possible to estimate an upper limit of η, by considering that the hologram absorbs half of the energy of the illuminating wave, resulting $\eta_T = 0.5$. In the image plane, 50% of the transmitted energy will be concentrated in the zeroth diffraction order, and only 25% of the transmitted light will form the signal because there is a twin signal. Thus the upper limit of η_D is 25%. As a result one obtain $\eta \leq 12.5\%$. In general η_T is significantly smaller than 50% for a gray-level hologram, and η may be much lower than the upper limit of 12.5%. The twin signal in the image plane is present due to the fact that amplitude holograms are real functions, and their Fourier transform must be Hermitian functions (Bracewell, 1986).

Image reconstruction error (root-mean-square deviation), e_i: During the IFTA, at the i-th iteraction, is the square root of the sum of the squares of the difference between the produced and desired intensities, with averaging summation performed over the entire domain of definition of image.

$$e_i = \frac{\sum_{m=-A/2}^{+(A/2)-1} \sum_{n=-B/2}^{+(B/2)-1} \left\{ \left| f_{mn} \right| - k_i \left| g^{*i}_{m+Mo,n+No} \right| \right\}^2}{AB}, \quad k_i = \frac{1}{\alpha_i} \tag{8}$$

$$\alpha_i = \frac{\sum_{m=-A/2}^{+(A/2)-1} \sum_{n=-B/2}^{+(B/2)-1} \left| g^{*i}_{mn} \right|^2}{\sum_{m=-A/2}^{+(A/2)-1} \sum_{n=-B/2}^{+(B/2)-1} \left\{ \left| f_{mn} \right| \times \left| g^{*i}_{m+Mo,n+No} \right| \right\}} \tag{9}$$

where the symbol (*) denotes the resulting image distribution after hologram constraints being applied in the i-th iteration.

Several parameters influence the minimization of the mean square error: the number of iterations, i, the pattern of the desired object (signal), the dimension of the reconstruction window, the degrees of freedom and the manner that the extra phase modulation operator is implemented (Wyrowski, 1990).

Signal-to-noise ratio, SNR: Another important parameter to evaluate the quality of the reconstructed signal, is the signal-to-noise ratio (*SNR*), defined by:

$$SNR = \frac{\sum_{m=-A/2}^{+(A/2)-1} \sum_{n=-B/2}^{+(B/2)-1} k_{final} \left| g_{mn}^{final} \right|^2}{AB \times e_{final}} \tag{10}$$

3. Implementation of computer-generated holograms

This section reports the design and fabrication of several digital holograms, from amplitude-only to full complex-amplitude modulation. In all cases the image generated is intensity-only objects. It also presents the implementation of a diffractive photomask applied to optical lithography and a diffractive lens with engineered Point Spread Function (PSF). The former diffractive element employs optical information processing to implement a spatial filter for target silhouettes applied to passive infrared motion sensors.

3.1 Amplitude-only modulation CGH: Fourier-type CGH, binary intensity-only object

In general it is difficult to implement the amplitude distribution of an amplitude-only CGH. Photographic film has nonlinearities which make difficult the control of the desired amplitude modulation and postscript printers generate amplitude modulation in a binary manner (half toning). Hence one is restricted to a binary amplitude modulation of the light, and the hologram elements can only assume the binary values *0* (when light is blocked) and *1* (when light passes through).

In the case of amplitude holograms one can assume that for the same signal there is a direct correspondence between the distribution of binary amplitude hologram and the distribution of a binary phase hologram (Wyrowski, 1990). Hence, during the coding of the hologram one can consider the binary amplitude hologram as a binary phase transmittance which can only have the complex value $1.exp[-j\pi] = -1$ and $1.exp[-j0] = +1$ ($j = (-1)^{1/2}$). By the addiction of a DC-term, it is possible to transform the resulting binary phase distribution into a binary amplitude distribution with values *0* and *1*. Since the hologram elements present only real values, the light distribution generated is Hermitian (Bracewell, 1986).

Figure 4 shows results of numerical and optical reconstructions of a pattern generated by a *64X64* pixels amplitude-only modulation hologram. The reconstruction plane has extension of *256X256* pixels. The hologram distribution can also be seen. The element was fabricated by using photographic film.

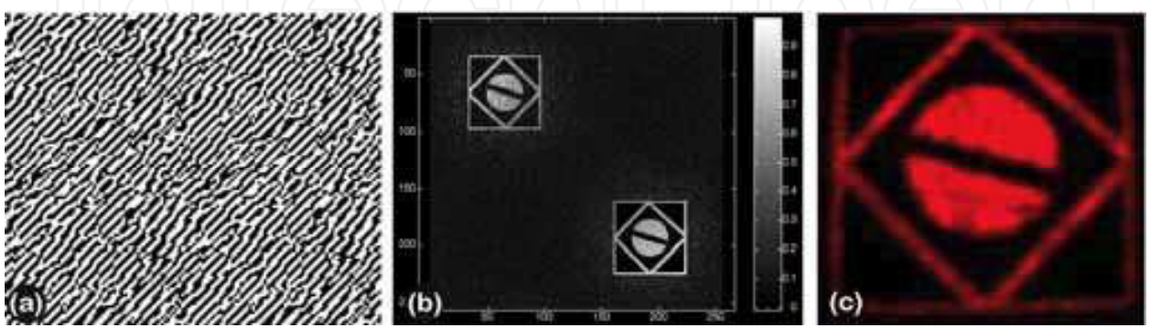

Fig. 4. (a) *64X64* pixels binary amplitude-only modulation hologram; (b) numerical reconstruction, with a reconstruction plane of *256X256* pixels; (c) Optical reconstruction. Only one image is shown; the DC central spot and the twin image were suppressed.

The main limitation in using a photographic film is the low diffraction efficiency achieved by an amplitude element, maximally of *12.5%*, if compared with the diffraction efficiency of about *90%* of a phase element (Wyrowski, 1990).
There are other methods to produce amplitude-only holograms such as Detour Phase Holograms, proposed by (Brown & Lohmann, 1969) and the Direct Binary Search, proposed by (Seldowitz, Allebach & Sweeney, 1987).

3.2 Phase-only modulation CGH: Fourier-type CGH, binary intensity-only object

Because the resulting inverse light propagation distribution $f(x',y')$ usually presents values of phase and amplitude modulation, this distribution must be adapted to the possible DOE distribution $g(x',y')$, which usually is a phase-only, due to its high diffraction efficiency. The use of phase modulation is attractive because no energy is absorbed by the hologram. A 2π phase modulation can be achieved in quantized values (O'Shea et al., 2004), or in continuous values (Turunen & Wyrowski, 1997; Herzig, 1997). If reduced quantized phase values are used, the problem of stagnation can arise during the iterative method. To overcome this limitation, the same IFTA algorithm (figure 2) can be used, with modifications to include the quantized phase values (Wyrowski, 1990).
Considering phase-only CGH, the IFTA method is started by placing the information of the object, f_{mn}, multiplied by random phase values, in the region of reconstructed window g_r. Since the hologram values are not restricted to real values, there is no twin image in the reconstruction plane, and g_r can be placed in its center. It is possible to improve the results for both amplitude- and phase-only CGHs by introducing corrections in the reconstruction window. The first correction, introduced by Wyrowski, takes account of the amplitude error from the previous reconstruction (Wyrowski, 1990a), and the second correction, introduced by Fienup, which includes a phase rotation operator inside g_r that tends to rotate the phase of the new input $g_{mn(i+1)}$ in the opposite direction to the phase of the old input $g_{mn(i)}$ (Fienup, 1980). Figure 5 shows optical reconstructed images, and microrelief profiles from binary phase-only CGH. Typical values for phase-only CGH are e_{final} = 2x10-3, η = 72% and SNR= 95.

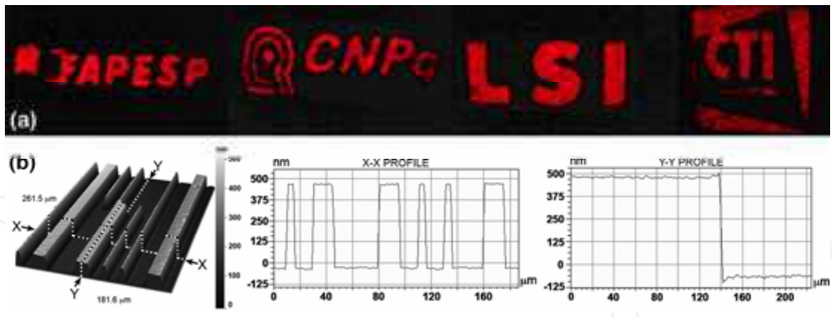

Fig. 5. (a) Optical reconstruction from binary phase-only CGH, (b) microrelief profiles obtained by interferometric microscopy technique. Reprinted with permission of Elsevier (Cirino, G. A. 2010).

3.3 Complex-amplitude modulation CGH: diffractive lithography photomask

The huge importance of the lithography on the fabrication of micro devices is well known. For most applications binary photolithography masks are employed. These masks consist of a transparent plate, covered by a patterned opaque film that acts as a light intensity modulating agent. The phase shift mask technique, introduced in the beginning of the eighties, employs a transparent thin film that modulates the phase of the transmitted light in

order to compensate the diffraction effect of the edges of the mask features (Levenson et al. 1982, Levenson 1993, 1994, 2006). In this application example, a phase shift diffractive proximity printing lithographic mask was designed, manufactured and tested (Cirino et al., 2010b). Its design is based on a Fresnel-type CGH, with phase and amplitude modulation, with a binary intensity-only object to be generated.
The proposed diffractive structure was designed to form the required image within a plane at *50 μm* behind the mask (distande *d* of figure 1b), onto a resist coated silicon wafer, as shown in figure 6. In this figure the mask is located in the plane *(x',y',z=0)*, and the wafer under exposure is located in the plane *(x,y,z=50μm)*. This inter-plane distance may be chosen as most suited for the used alignment equipment. This gives another important degree of freedom for this procedure, optimizing the resolution of the transferred patterns for specific equipment.

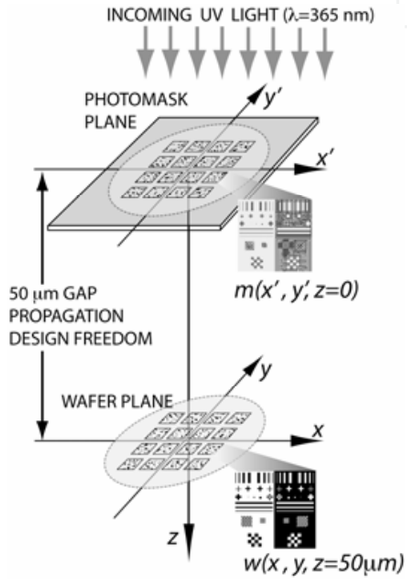

Fig. 6. Schematic view of the optical field projected by the mask, when illuminated by a UV plane wave. The pattern is obtained by applying free space light propagation along the *50 μm* distance. Reprinted with permission of OSA (Cirino, G. A., 2010).

The obtained amplitude and phase distributions were mapped into discrete levels. A coding scheme using sub-cells structure was employed in order to increase the number of discrete levels, thus increasing the degree of freedom in the resulting mask. The results show an improvement of the achieved resolution – linewidth as good as *1.5 μm* - what is impossible to obtain with traditional binary masks in proximity printing mode.
The photomask was fabricated by binary optics (O'Shea et al., 2004) and the sub-cells-based coding scheme was introduced to increase the design degree of freedom. Another contribution of this work is the employment of an a:C-H thin film to modulate the light amplitude. The amorphous carbon layer blocks the light only in the UV region, being partially transparent in the visible region of the spectrum. This characteristic makes mask alignment much easier. A fused silica substrate is used to modulate the phase and the a:C-H layer to modulate the intensity of the incoming UV light plane wave.
In order to give additional degree of freedom and expand the possible values attributed to the complex transmittance of the mask, consider the cells of the photomask shown in figure 7. The cell centers are spaced at regular intervals of width X in the x' direction and regular intervals of width Y in the y' direction. Since each cell is divided in sub-cells, it is possible to deal with

the relation between areas that assume two different values of phase and/or amplitude inside this cell.

Consider, for example, the first quarter of complex plane. Figure 7 illustrates the subdivision of a cell, formed by 4×4 sub-cells, with new possible values of phase and amplitude. Figure 7a shows the structure of a particular cell that can modulate the phase between *0* and $\pi/2$. Intermediate phase values of the function $\phi(x',y')$, distributed between *0* and $\pi/2$, can be approximated by combining different regions inside the cell.

The variation of *V*, from *0* to *Y* inside the cell will introduce a smooth phase variation from *0* to $\pi/2$ radians.

Figure 7b shows the structure of a window created on top of the phase cell of figure 7a, in order to modulate the amplitude of incident light between *0* and *1*. The variation of *U*, from *0* to *X* inside the cell will introduce a smooth amplitude variation from *0* to *1*.

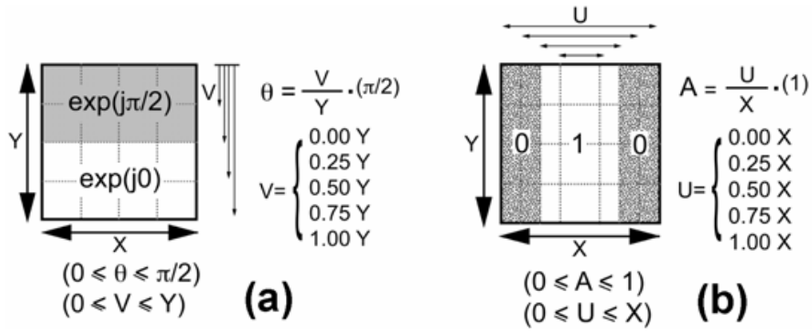

Fig. 7. Subdivision of a cell, formed by 4×4 sub-cells. (a) structure of a particular cell that can modulate the phase between *0* and $\pi/2$, depending of the value of *V*; (b) structure of a window created over the phase cell of figure 7a, in order to modulate the amplitude of incident light between *0* and *1*, depending of the value of *U*. Reprinted with permission of OSA (Cirino, G. A., 2010).

Figure 8a shows the structure of a particular cell with complex transmittance of amplitude equal to *0.5* and phase equal to $\pi/4$. Figure 8b shows all the possible values (black dots) of amplitude and phase within the first quadrant, as well as, the particular value of the cell of figure 8a. The full complex-amplitude modulation is achieved on the entire complex plane, i.e., on the regions of second, third and fourth quadrant, by combining, respectively, phase values $\pi/2$-π, π-$3\pi/2$, and $3\pi/2$-*0*.

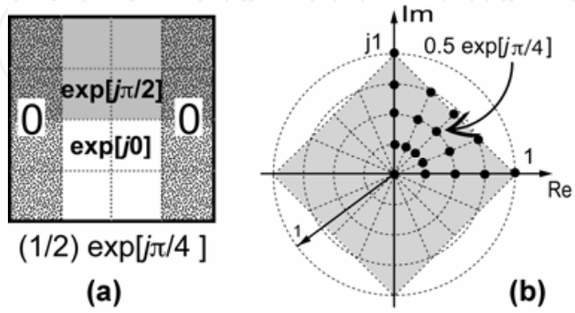

Fig. 8. (a) Structure of a particular cell with complex transmittance of amplitude equal to *0.5* and phase equal to $\pi/4$; (b) all the possible value (black dots) of amplitude and phase within the first quadrant, as well as, the particular value of the cell of figure (a). Reprinted with permission of OSA (Cirino, G. A., 2010).

To generate the optical reconstruction, the scalar diffraction theory was employed, by considering the free space propagation of the light along the gap between mask and wafer planes. The mask was designed by the inverse propagation of light. In this method, the desired complex distribution of the mask *m(x',y',z=0) = w(x',y',z=0)* is obtained by solving the Helmholtz equation $(\nabla^2 + k^2)w(x,y,z) = 0$ in the frequency domain for a predefined intensity light distribution *w(x,y,z=50μm)*, which must be present in the wafer plane, as shown in figure 6.

The application of the requirement above shows that *W(fx,fy,z=50μm)* must satisfy the differential equation (Goodman, 1996):

$$\frac{\partial^2}{\partial z^2} W\left(f_x, f_y, z\right) + \left(\frac{2\pi}{\lambda}\right)^2 \left[\, 1 - \left(\lambda f_x\right)^2 - \left(\lambda f_y\right)^2 \,\right] W\left(f_x, f_y, z\right) = 0 \qquad (11)$$

An elementary solution of this equation, in the frequency space, can be written in the form:

$$W\left(f_x, f_y, z\right) = M\left(f_x, f_y, 0\right) \exp\left[j\frac{2\pi}{\lambda} z \sqrt{1 - \left(\lambda f_x\right)^2 - \left(\lambda f_y\right)^2} \right], \; j = \sqrt{-1} \qquad (12)$$

where *W(fx,fy,z=50μm)* and *W(fx,fy,z=0) = M(fx,fy,z=0)* are the two-dimensional Fourier transform of the functions *w(x,y,z=50μm)* and *m(x',y',z=0)*, respectively; f_x and f_y are the frequency coordinates in the *x* and *y* directions, respectively. Equation 12 describes, in the frequency space, the relation between the desired light distribution in the wafer plane *w(x,y,z=50μm)* and the diffraction structure in the mask plane, *m(x',y',z=0)*.

From the above result, the propagation phenomenon may be regarded as a linear, dispersive spatial filter with a finite bandwidth of extension inside a circular region with radius λ^{-1} in the frequency plane. Its transfer function, $H(f_x,f_y)$, is given by

$$H\left(f_x, f_y\right) = \begin{cases} \exp\left[j\frac{2\pi}{\lambda} z \sqrt{1 - \left(\lambda f_x\right)^2 - \left(\lambda f_y\right)^2} \right] & \text{for} \quad \sqrt{\left(f_x\right)^2 + \left(f_y\right)^2} < \frac{1}{\lambda} \\ 0 \quad \text{otherwise} \end{cases} \qquad (13)$$

Figure 9 shows a schematic diagram of the phenomenon of free space propagation, and its relation with frequency and image spaces, as well as mask and wafer planes.

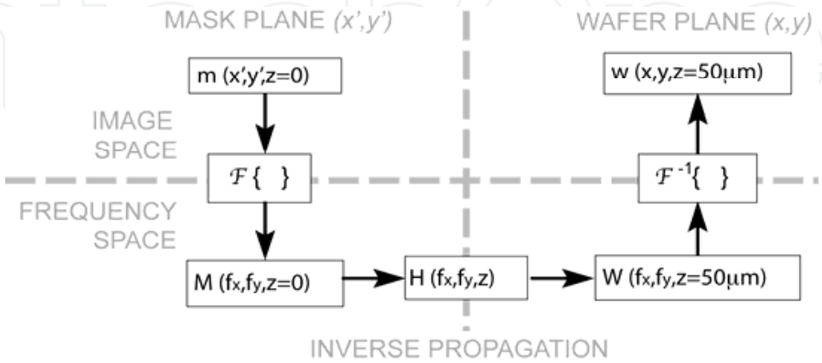

Fig. 9. Schematic diagram of the phenomenon of free space propagation, and its relation with frequency and image spaces, as well as mask and wafer planes. Reprinted with permission of OSA (Cirino, G. A., 2010).

To calculate the inverse propagation from the wafer plane to the mask plane, one has to apply the inverse filter for propagation:

$$m(x',y',z=0)=\Im^{-1}\left\{\frac{W\left(f_x\ ,f_y\ ,z=50\mu\mathrm{m}\right)}{\exp\left[j\frac{2\pi}{\lambda}z\sqrt{1-\left(\lambda f_x\right)^2-\left(\lambda f_y\right)^2}\right]}\right\} \tag{14}$$

where $\Im\{.\}$ denotes the two-dimensional Fourier transform operator.
In the calculation of the inverse light propagation, the following normalized function, $m_N(x',y')$, is considered,

$$m_N\left(x',y'\right)=\beta\ m\left(x',y'\right)=A\left(x',y'\right)\exp\left[j\phi\left(x',y'\right)\right] \tag{15}$$

where $A(x',y') = |m(x',y')|$ is the amplitude $[0 \le A(x',y') \le 1]$, $\phi(x',y')$ is the phase distribution $[0 \le \phi(x',y') \le 2\pi]$, $\beta = 1/\{MAX\ [m(x',y')]\}$ is a scale factor (a real number) used to normalize the maximum amplitude of $|m(x',y')|$ to unity, and the operator $MAX[.]$ represents the maximum value of the function $m(x',y')$. In the design, the desired reconstruction is a real distribution $w(x,y,z=0) = |w(x,y,z=0)|\ exp[j0]$.
The diffractive phase shift mask is considered as a two-dimensional matrix structure with $M \times N$ rectangular cells of dimensions $X \times Y$, with M and N being even numbers. Each cell represents a complex transmittance value $m_{kl}(x',y')$ with $[(-M/2) \le k \le ((M/2)-1)]$ and $[(-N/2) \le l \le ((N/2)-1)]$.
The phase and amplitude information must be mapped into the discrete values:

$$A\left(x',y'\right)\exp\left[j\phi\left(x',y'\right)\right]\ \leftrightarrow\ A_{kl}\left(x',y'\right)\exp\left[j\theta_{kl}\left(x',y'\right)\right] \tag{16}$$

Considering the cell structure described above and supposing that the mask is placed in the (x',y') plane, the mathematical representation of the diffractive mask in terms of Fourier optics is given by:

$$m_{kl}\left(x',y'\right)=rect\left(\frac{x'}{MX},\frac{y'}{NY}\right)\left\{\sum_{k=-M/2}^{M/2-1}\sum_{l=-N/2}^{N/2-1}rect\left(\frac{x'-kX}{A_{kl}}\right)\left[\begin{array}{l}rect\left(\dfrac{y'-lY}{Y}\right)+\\ \left(e^{j\pi/2}-1\right)\ rect\left(\dfrac{y'-Y\left(\dfrac{1}{2}-\dfrac{\theta_{kl}}{\pi}\right)-lY}{Y-\dfrac{2\theta_{kl}}{\pi}}\right)\end{array}\right]\right\} \tag{17}$$

Figure 10a shows the intensity distribution of a test structure desired to be transferred to the wafer, $w(x,y,z=50\mu m)$; figures 10b and 10c show the corresponding amplitude distribution, $A(x',y')\ [0<A<1]$, and phase distribution, $\phi(x',y')\ [0<\phi<2\pi]$, to be implemented in the mask after applying the propagation method described above.

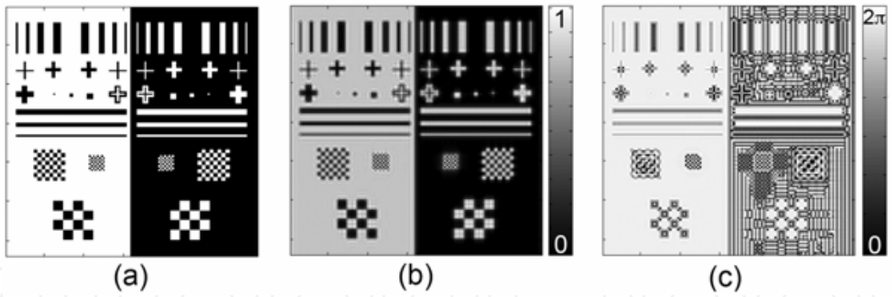

Fig. 10. Lithographic test structures used to show the basic idea of the complex-amplitude modulation proximity printing mask. (a) Numerical reconstructed image of the desired light distribution; (b) amplitude $A(x',y')$ and (c) phase $\phi(x',y')$ distributions of the resulting phase shift photomask. Reprinted with permission of OSA (Cirino, G. A., 2010).

Figure 11 shows schematically the entire process to fabricate the proposed diffractive phase shift proximity photomask.

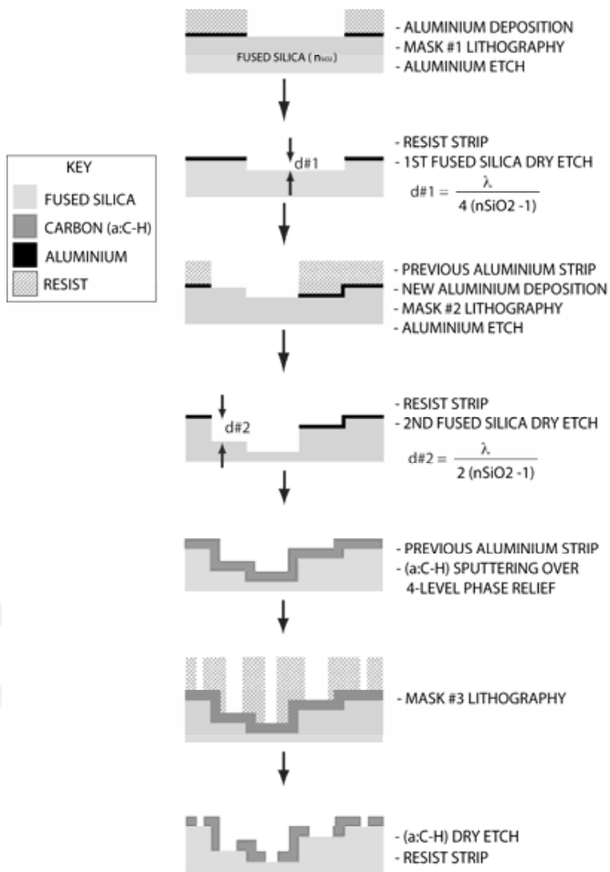

Fig. 11. Schematic view of the entire process to fabricate the proposed diffractive phase shift proximity photomask. Reprinted with permission of OSA (Cirino, G. A., 2010).

The phase shift diffractive photomask was implemented using the discrete phase and amplitude informations. The phase distribution was transferred by generating a variation of the thickness $d_{kl}(x',y')$ on a fused silica substrate with refractive index n_{SiO2}, using the relation

$$d_{kl}(x',y') = \frac{\theta_{kl}(x',y')}{2\pi} \frac{\lambda}{(n_{SiO2} - 1)} \tag{18}$$

where $\lambda = 365nm$ is the operating wavelength of the exposure light source.
This variable thickness was approximated by using binary optics (O'Shea et al., 2004), with four phase-levels.
To implement the amplitude modulation in this phase shift diffractive mask, an a:C-H layer is deposited on top of the SiO2 four-level phase relief, and patterned by a third lithographic mask (mask #3 in figure 11), generating the variable apertures size over the region of each phase pixel structure previously patterned. It should be mentioned that this carbon layer is opaque at $\lambda = 365\ nm$, and relatively transparent in the visible region of the spectrum.
Figure 12 shows part of the test structures with a detail of a line 1.5 μm wide by *82 μm* length, patterned in proximity (*50 μm* gap) and contact modes. One can note that the line obtained by proximity exposure is clearly resolved while that obtained by contact exposure is barely resolved.

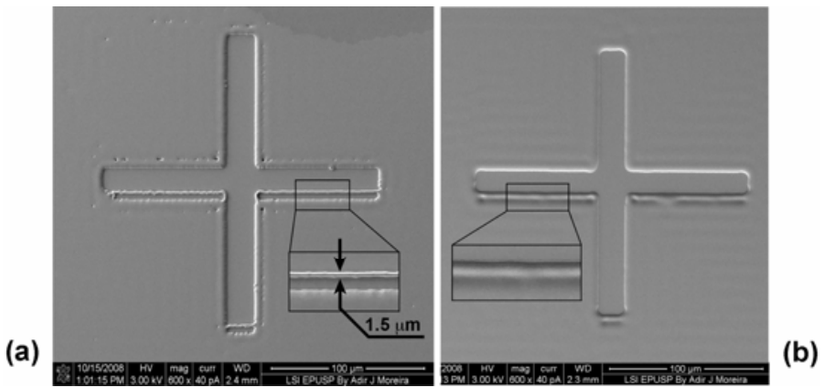

Fig. 12. SEM micrographs of part of the test structures with a detail of a line *1.5 μm* wide by *82 μm* length, patterned in (a) proximity (*50 μm* gap) and (b) contact modes. The line obtained by proximity exposure is clearly resolved while that obtained by contact exposure is barely resolved. Reprinted with permission of OSA (Cirino, G. A., 2010).

3.4 Complex-amplitude modulation CGH: Fresnel-type CGH, gray-tone intensity-only object

In this section a Fresnel-type CGH with a graytone intensity-only object was designed and fabricated (Neto et al., 2003,2004). The calculations procedure are the same as previous section.
A hologram was designed considering the reconstruction plane located of *1.2* meters from the hologram (distance *d* of figure 1b). Here again, the desired reconstruction was a real distribution $f(x,y,0) = |f(x,y,0)|.\ exp\ (j0)$ with smooth variations intensity (gray-tone diffraction pattern). The hologram pixel size is *40 μm* by *40 μm* and the total hologram size is *1024 μm* by *1024 μm*.
In figure 13 are shown the desired reconstruction distribution $f(x,y,d)$ together with its corresponding phase and amplitude distributions, obtained after applying the propagation methods described in the previous section.
The complete device fabrication sequence is shown schematically in figure 14a. All the used process steps are well controlled and well known for micromechanical and microelectronic applications. The fabrication is based on DLC thin film, with four phase level surface relief. After the reactive ion etching, a reflective aluminum layer is deposited over the phase relief

using a thermal evaporation process. The amplitude modulation is achieved by removing small parts of this reflective aluminum layer over the region of each phase pixel. The area of these apertures must be proportional to the amplitude $|G_{kl}|$., following the sampling scheme described in equations 1-4.

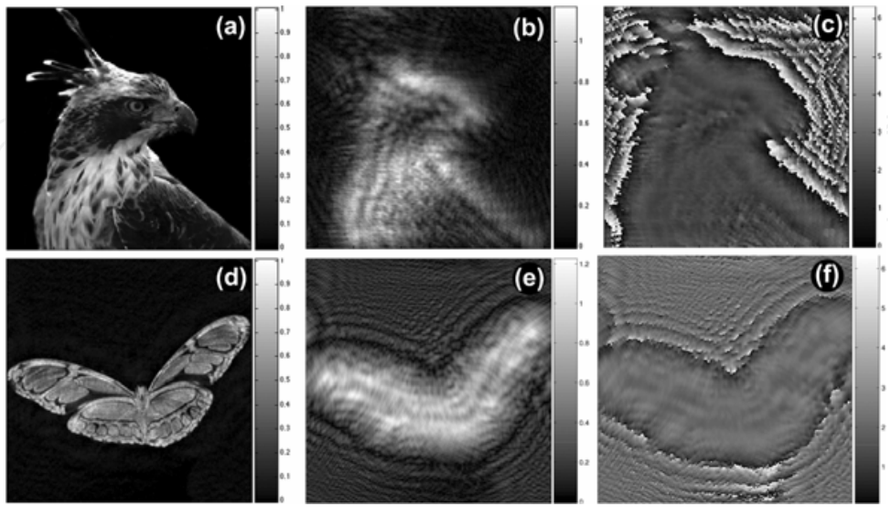

Fig. 13. (a&d) Image of the desired light wave front distribution $f(x,y,z) = =|f(x,y)|exp[i\varphi(x,y)]$, (b&e) amplitude ($0 \leq |f(x,y)| \leq 1$) and (c&f) phase distribution of the resulting Fresnel hologram, ($0 \leq \varphi(x,y) \leq 2\pi$). Reprinted with permission of SPIE (Neto, L. G., 2004).

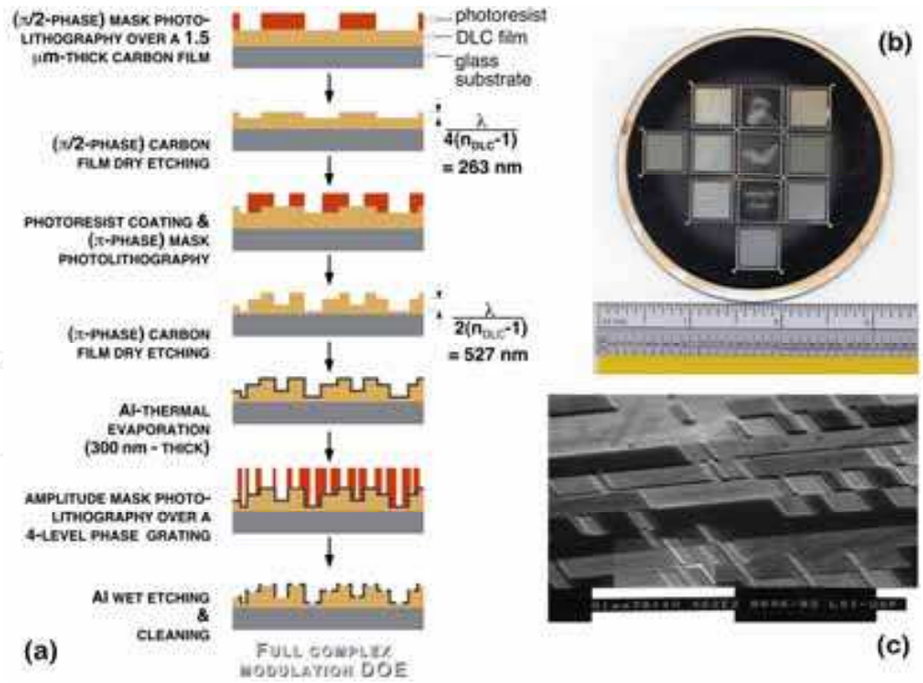

Fig. 14. (a) Schematic view of the fabrication of the full complex amplitude modulation CGH; (b) 3-inch diameter glass substrate, with 12 different CGHs fabricated. (c) Scanning electron microscope picture with details of the geometry of the rectangular pixels. Reprinted with permission of SPIE (Neto, L. G., 2004).

A photolithographic mask with apertures over the region of each phase pixel was fabricated considering the amplitude distribution $|G_{kl}|$.
Each value of $|G_{kl}|$, $(0 \leq |G_{kl}| \leq 1)$, is coded in a 8×8 cell, positioned over each respective pixel of phase. With the used mask set, 11 different DOEs onto a 3-inch diameter glass substrate were fabricated. A photography of a 3 inch wafer with the fabricated elements is shown in Fig. 14b, and a micrograph with details of the geometry of a rectangular pixel that forms the hologram structure, is shown in Fig. 14bc
Figure 15 compares the desired reconstruction $f(x,y,d)$ of Fig. 13a with the optical reconstruction of the Fresnel hologram fabricated using the amplitude and phase information of Figs. 13b and 13c. Because a constant phase distribution is assumed in the reconstruction plane (the desired reconstruction is a real distribution), no speckle noise is present in the optical reconstruction.

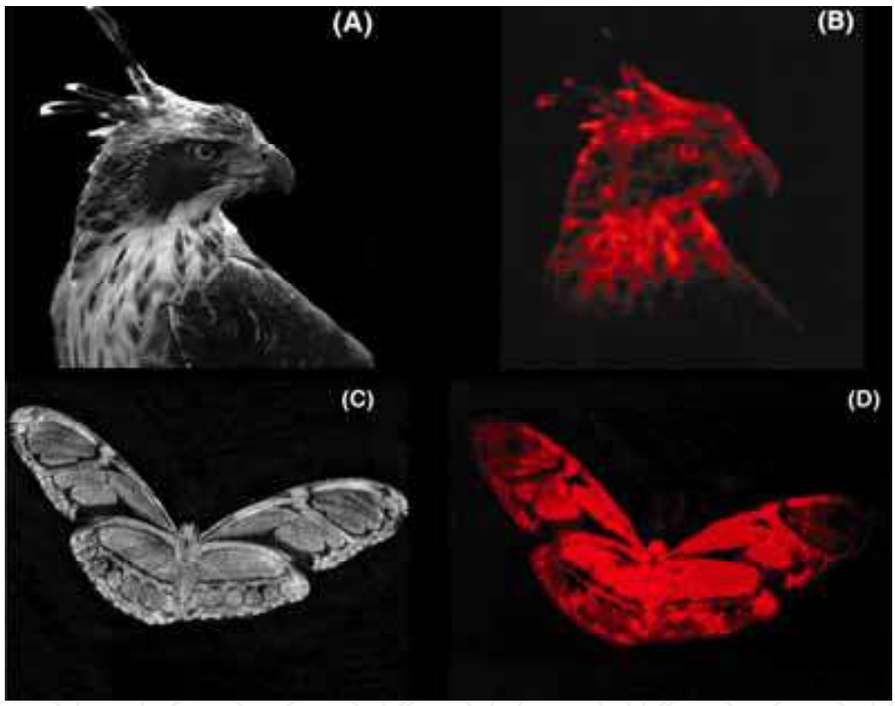

Fig. 15. Comparison between the desired and the obtained reconstructions of a gray-tone object. (a&c) Numerical distribution $f(x,y,d)$, (b&d) optical reconstruction of the Fresnel CGH fabricated using the amplitude and phase information of Figs. 13b and 13c. Reprinted with permission of SPIE (Neto, L. G., 2004).

For comparison purpose, figure 16a shows the phase distribution of a phase-only CGH designed using one hundred iterations of the IFTA, for the same desired image shown in Fig. 13a. The reconstruction plane was also located *1.2* meters away from the element. A random phase distribution was attributed to in the first iteration. The phase-only CGH was manufactured using a similar process sequence described above (of course, without the process steps concerning the third mask which determines the aluminum features).
Figure 16b shows the computer reconstruction of the phase-only element and Fig. 16c shows its optical reconstruction: a strong speckle noise is present in the optical reconstruction.

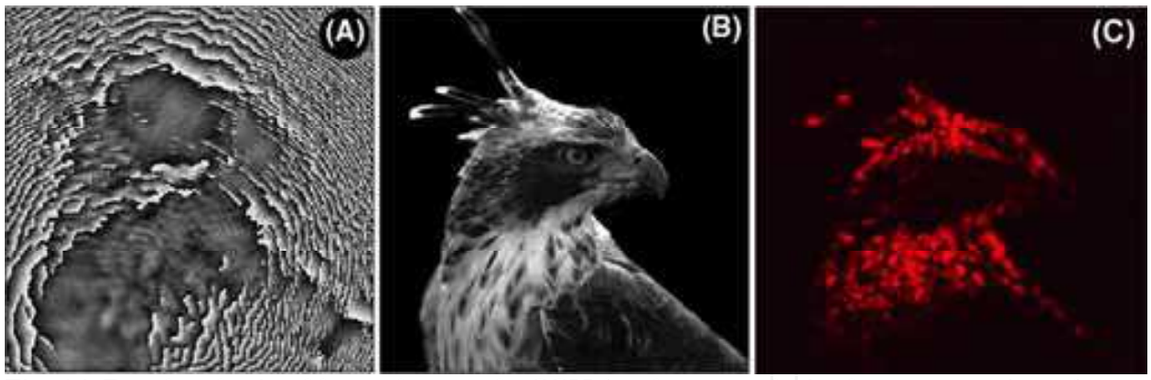

Fig. 16. Results obtained by a phase-only CGH for the same desired reconstruction of figure 13 (a) phase distribution of the CGH, designed using one hundred iterations of the IFTA for the desired image shown in Fig. 13a, (b) computer reconstruction, (c) optical reconstruction: a strong speckle noise is present. Reprinted with permission of SPIE (Neto, L. G., 2004).

The comparison between figures 15b and 16c indicate clearly the superiority of the new element over the traditional phase only DOE. The improved optical performance is caused by the total freedom in the design assured by the full complex amplitude modulation. Naturally, the diffraction efficiency of figure 16b is lower than that of figure 17c, due to the amplitude modulation mask (figure 13b), which blocks a significant portion of the incoming wavefront.

3.5 Complex-amplitude modulation CGH: Fourier-type CGH, binary intensity-only object

In this example a binary, intensity-only image is generated, considering nine levels of amplitude modulation and four levels of phase modulation as a constraint in the hologram plane. The reconstruction window g_r (signal window) in the reconstruction plane has the same space-bandwidth product of the hologram, i.e., one has no complex amplitude freedom in the reconstruction plane. In this plane one has only phase freedom assuming the object is a intensity-only distribution. After 100 iterations, the resulting *128X128* complex amplitude hologram $G_{kl} = |G_{kl}| \, exp(j\phi_{kl})$,with $(0 \leq |G_{kl}| \leq 1)$, $\phi_{kl} = (0, \pi/2, 2\pi/2, 3\pi/2)$ and $(1 \leq k,l \leq 128)$, is obtained. The diffraction efficiency of the transmitted energy, considering equation 7, is $\eta_T \cong 22\%$. The quality of the resulting complex amplitude hologram G_{kl} is measured using the mean square error function, defined by equation 8, which compares the final hologram's reconstruction g_{mn} with the desired reconstruction f_{mn} is $e_{final} = 2.1 \times 10^{-3}$.

The resulting phase distribution was used in the fabrication, here again, based on sputtered carbon thin film, with four phase level surface relief, as described in the previous section. Figure 17a shows the complex-amplitude transmittance of the resulting hologram. Here again, it presents a sub-cell approach design, which enable an increase in the degree of freedom in the coding of complex distributions in the hologram media, resulting in high quality images (diffraction patterns). Figures 17b and 17c shows the intensity of the computer reconstruction compared to the intensity of its optical reconstruction.

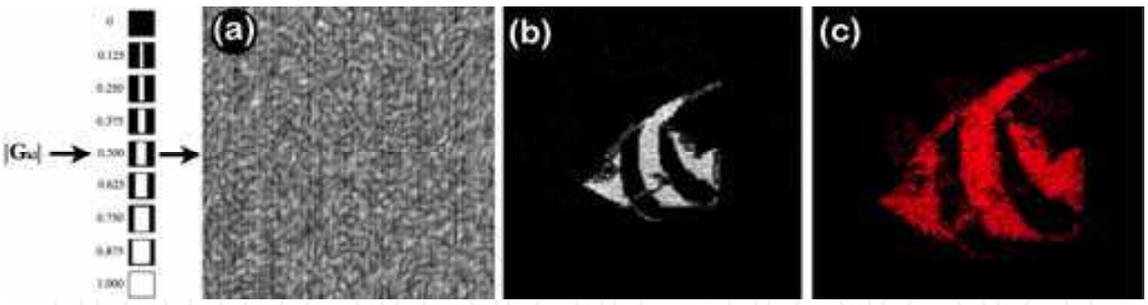

Fig. 17. (a) Coding of each value of $|G_{kl}|$, $(0 \leq |G_{kl}| \leq 1)$ in a 8×8 cell, positioned over each respective pixel of phase, (b-c) comparison between (left) the intensity of the hologram computer reconstruction g_{mn} and (right) the intensity of its optical reconstruction.

3.6 Optical information processing: Silhouette filtering by a diffractive lens

Passive InfraRed (PIR) motion sensors have been extensively used in electronic monitoring of assets in domestic and corporative security applications. Its principle of operation is based on the employment of a pyroelectric detector, which is responsible for transducing an incident IR radiation (*8-14 μm* wavelength range) to an electric signal.

In this application, the engineered Point Spread Function (PSF) concept of optical systems using cubic phase distribution was applied, in order to implement an optical image filtering in the design of inexpensive Fresnel lenses array for PIR motion sensors. The goal is to perform, in a purely optical approach, the so-called pet immunity feature, i.e., the sensor must detect humans, filtering and neglecting the information generated by small pets (Cirino, 2003, 2004).

Imaging systems that use incoherent illumination obey the intensity convolution integral (Goodman, 1996):

$$I_{out}(x,y) = \int_{-\infty}^{\infty} \left| h(x-u, y-v) \right|^2 I_G(u,v)\, du dv \tag{19}$$

where $I_G(u,y)$ is the intensity of the image predicted by geometrical optics for each lens of the lenses array, $h(x,y,u,v)$ is the PSF, or the impulse response of the lens and $I_{Out}(x,y)$ is the intensity of the output image formed by the lens. u and v are the coordinates in the spatial frequency space in the x- and y-directions, respectively. Thus in this general case, one can regard the output image as being a convolution of the image predicted by geometrical optics with the intensity of the PSF of the system. Narrow PSF results in optical system with the ability to resolve higher spatial frequencies compared to a system with a wide PSF.

Considering only the vertical y-direction, human silhouettes have lower spatial frequencies compared to small pets. In order to assure the distinction, a one-dimensional vertical cubic phase distribution $P_Y(y)$ is superimposed to the conventional quadratic phase distribution of each lens. $P_Y(y)$ is defined by (Dowski, 1995):

$$P_Y(y) = \exp(j\sigma\, y^3) \tag{20}$$

where σ is the cubic phase factor. The multiplication of the spherical phase distribution of each lens by the cubic phase $P_Y(y)$ spreads the resulting PSF. Considering equation 19, the

convolution of $I_G(u,y)$ with the intensity of a wide PSF performs a low-pass spatial filtering in the y-direction.

Figure 18a shows the input test image used in the computer simulation. Figure 18b shows the resulting distribution using equation 19, and figure 18c shows its corresponding PSF. One can note from fig.3b that, thanks to this particular PSF distribution, the image of the human body has a higher intensity distribution compared to the image of the small pet.

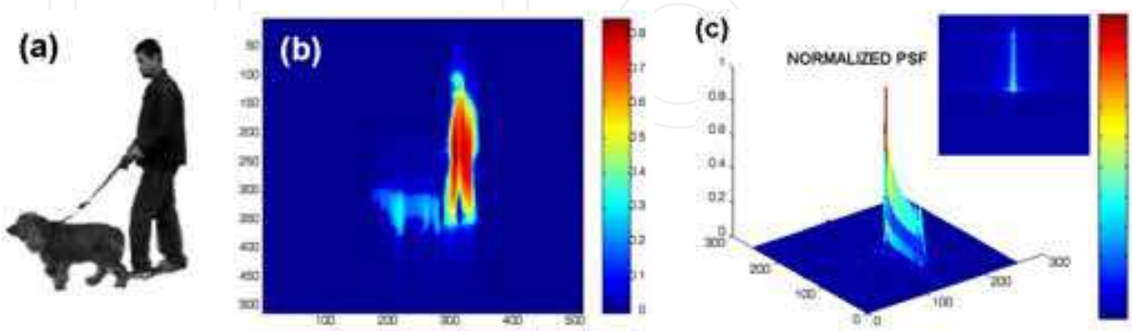

Fig. 18. Numerical simulation of the performance of the cubic phase mask to be embedded in the sensor's Fresnel lens array (a) Input test image used in the computer simulation; (b) corresponding simulated output image, normalized to its maximum value; (c) normalized PSF distribution of the optical system. One can note that the image of the human silhouette has higher brightness when compared to the image of a small pet.

In order to show how the lens can be employed in the distinction of human targets from pet targets, a lens set on Diamond-Like Carbon (DLC) thin film were designed and manufactured by microfabrication process techniques (Cirino, 2004; Goodman 1996). Although the sensor operates at the *8-14 μm* wavelength range, a diffractive Fresnel lens which operates in the visible portion of the spectrum was fabricated, with a central wavelength of *500 nm*. This is a suitable way to show that the principle works, being directly applied in the desired wavelength range (mid infra-red). For comparative purposes, besides each cubic-phase distribution Fresnel lens, a conventional quadratic Fresnel lens was also fabricated. Both lenses were submitted to the same process steps during the whole fabrication process. The lenses microrelief were fabricated on the *1.5 μm*-thick DLC thin film, using the following relation

$$th(x_P, y_P) = \frac{\lambda}{2\pi(n_{DLC} - 1)} \phi(x_P, y_P) \tag{21}$$

where $th(x_p,y_p)$ is the thickness variation within the transparent carbon film, $\lambda = 500\,nm$ is the operating wavelength, n_{DLC} is the refractive index of the *DLC* layer (measured at wavelength λ) and $\phi(x_p,y_p)$ is the phase distribution information $[0 \le \phi(x_p,y_p) \le 2\pi]$ (Herzig, 1997).

Figure 19 shows schematically the experimental set up employed to perform the comparative tests. The object, located in the back focal plane of the lens, at a distance z_i, is illuminated by a diffused incoherent white light source. The lens produces the image of the object directly in the plane of a CCD camera, located at a distance z_a from the lens.

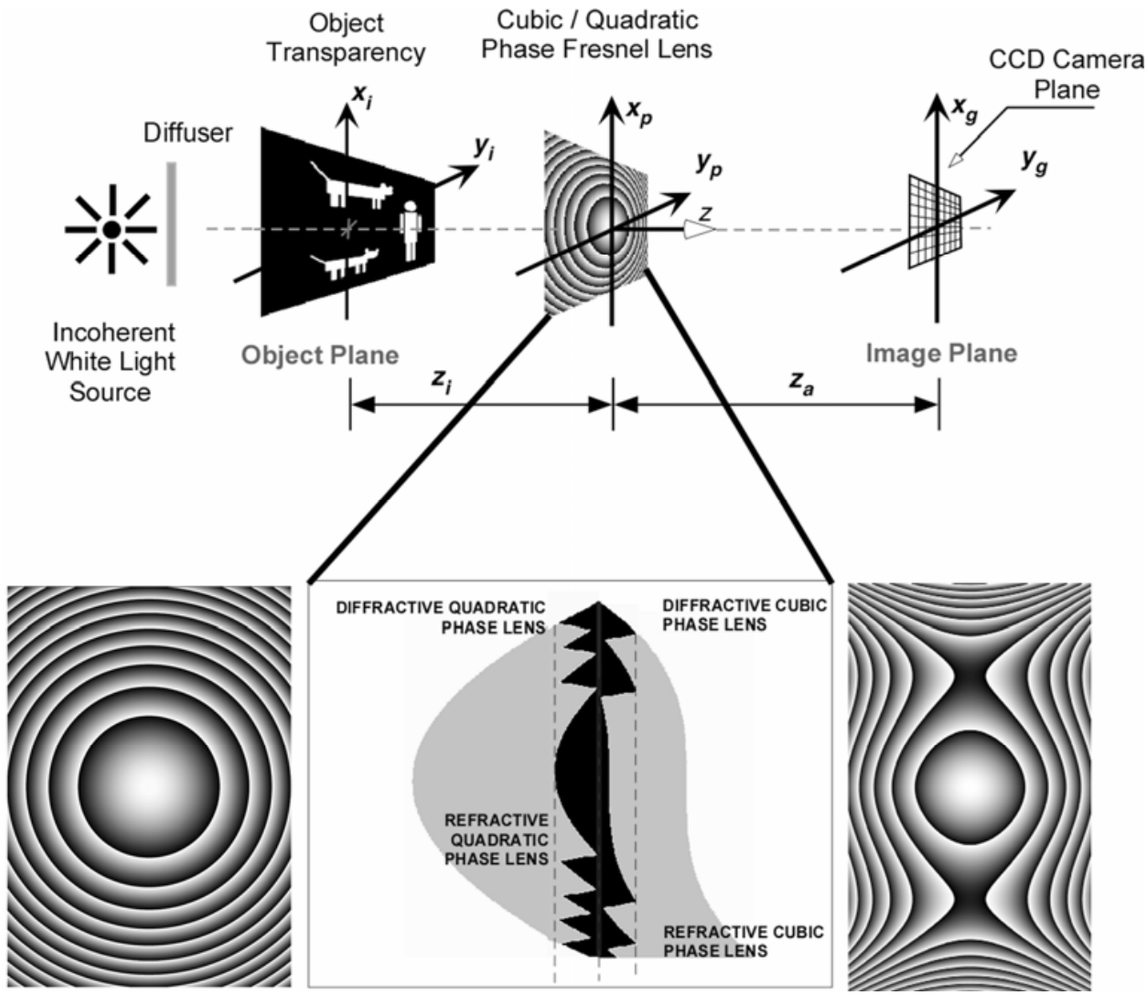

Fig. 19. Experimental set up employed to store the images produced by the fabricated Fresnel lenses. The object plane is illuminated by a diffused incoherent white light source and the lens images the object directly in the CCD plane of the camera. Details of the quadratic and cubic phase distributions are also shown.

Figure 20a and 20b show the resulting images from the conventional lens (quadratic phase profile) and the proposed lens (cubic phase profile), respectively. One can see that cubic phase profile spreads the light as predicted by the simulated results. The optical power generated by pet targets is attenuated (to a value of about 50% of the maximum value), as compared with human targets. Therefore this approach can be used to allow some blurring of the PSF of the optical system in such a way that it turns possible the discrimination between humans and pets for passive infrared motion sensor applications.

4. Conclusions

In this chapter some aspects of digital holography were delineated. An iterative method based on the fast Fourier transform was presented, which permits the design of diffractive optical elements in the scalar domain.

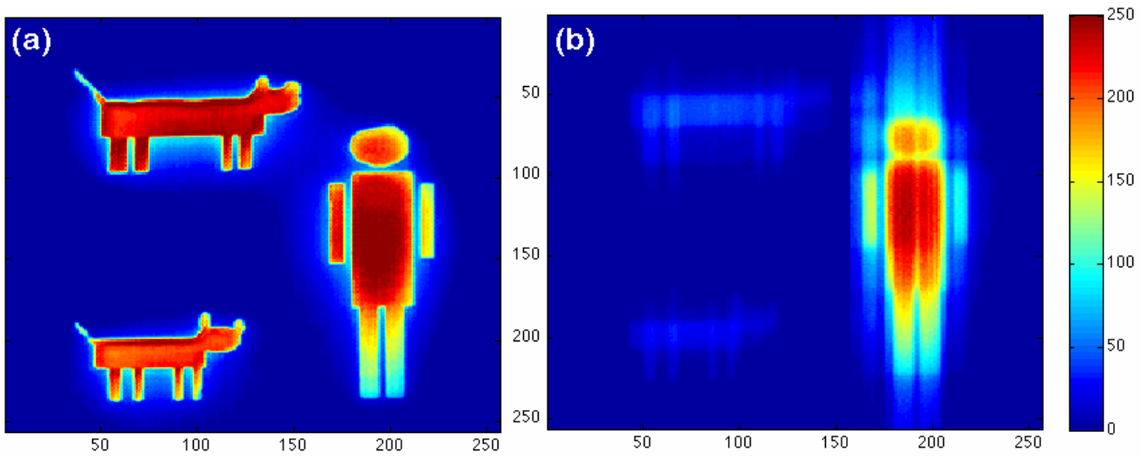

Fig. 20. Resulting intensity images generated from the Fresnel lenses in the visible range of spectrum. (a) Resulting image from the conventional (quadratic phase profile) lens; (b) resulting image from the proposed lens (cubic phase profile). One can note the enhancement of the human body intensity distribution

Several examples of Fresnel- and Fraunhofer-type holograms as well as amplitude-only, phase-only and full complex-amplitude modulation devices were presented to illustrate the potential of this technology in the generation of high quality diffraction patterns. A fabrication technique based on a patented carbon thin film process was employed. Among the applications, a diffractive photomask and a diffractive lens with a cubic phase distribution were presented. The first application enables one to increase the resolution of features to be transfer to a silicon wafer when operating in proximity printing mode lithography. The second one was used to implement a low-pass filter in order to make a distinction of human silhouettes from those of small pets for passive infrared motion sensors applications.

5. Acknowledgment

The authors would like to thank CTI for the fabrication of the photolithographic masks, and the agencies Conselho Nacional de Desenvolvimento Cientfico e Tecnológico (CNPq), process # 151908/2007-9, and Fundação de Amparo à Pesquisa no Estado de São Paulo (FAPESP), grants # 98/02755-7 ; 00/10181-2 ; 00/11117-6 and 02/07840-0. This work is part of the Instituto Nacional de Ciência e Tecnologia: Óptica e Fotônica (INCT-INOF), sponsored by CNPq (grant # 573587/2008-6) and FAPESP (grant # 08/57858-9).

6. References

Benton, S. A. (1969) On a method for reducing the information content of holograms, *Journal of Optical Society of America*, Vol. 59, pp. 1545-1551, ISSN 0030-3941

Bracewell, R. N., (1986), *The Fourier Transform and Its Applications*, McGraw Hill Series in Electrical Engineering, ISBN 0-0730-3938-1, Massachusetts, USA

Brown, B.R. & Lohmann, A.W. (1966) Complex spatial filtering with binary masks, *Applied Optics* (June 1966), v.5, n.6, p.967-969, ISSN 2155-3165

Brown, B. R.; Lohmann, A. W. (1969a) Computer-generated binary holograms, *IBM Journal of Research and Development*, v.13, pp. 160-168, ISSN 0018-8646

Brown, B.R. & Lohmann, A.W. (1969b)"Computer-generated binary holograms", *IBM Journal of Research and Development* (May 1969), v.13, p. 160-168, ISSN 0018-8646

Cirino, G. A. & Neto, L. G. (2003), Design of cubic distribution lenses for passive infrared motion sensors, *Proceedings SPIE 5073 of the XXV Thermosense*, pp. 476–484, ISBN 0-8194-4932-6, Orlando, Florida, USA, April 22-24, 2003

Cirino, G. A. & Neto, L. G. (2004), Optical implementation of cubic-phase distribution lenses for passive infrared motion sensors, *Proceedings SPIE 5405 of the XXVI Thermosense*, pp. 189–198, ISBN 0-8194-5328-5, Orlando, Florida, USA, April 13-15, 2004

Cirino, G. A.; R. D. Mansano; P. Verdonck, L. Cescato, & L. G. Neto (2010a), Diffractive phase-shift lithography photomask operating in proximity printing mode, *Optics Express* (August 2010), Vol. 18, Issue 16, pp. 16387-16405, ISSN 1094-4087

Cirino, G. A.; R. D. Mansano; P. Verdonck, R. G. Jasinevicius, & L. G. Neto (2010b), Diffraction gratings fabricated in DLC thin films, *Surface & Coatings Technology* (June 2010), Vol. 204, No. 18-19, pp. 16387-16405, ISSN 0257-8972

Cooley, J. W. & Tukey, J. W. (1965) An Algorithm for the Machine Calculation of Complex Fourier Series, *Mathematics of Computation*, vol. 19, No. 90, pp. 297–301, ISSN 1088-684

Denisyuk, Y. N. (1962) . Photographic reconstruction of the optical properties of an object in its own scattered radiation field. *Soviety Physics - Doklady*, Vol. 7, pp. 543-549, ISSN 0038-5689

Dowski Jr., E. R. & Cathey, W. T. (1995), Extended depth of field through wave-front coding, *Applied Optics,* Vol. 34 No. 11, pp. 1859-1866, ISSN 2155-3165

Fienup, J. R. (1980), Iterative method applied to image reconstruction and computer-generated holograms, *Optical Engineering* (June 1985), Vol. 19, No. 3, pp. 297-305, ISSN 0091-3286

Gabor, D (1948) A new microscopic principle, *Nature* (1948), Vol. 161, pp. 777-778, ISSN 0028-0836

Goodman, J. W. (1996), *Introduction to Fourier Optics*, pp. 55-61, McGraw Hill, ISBN 0-07-024254-2, New York, USA

Herzig, H. P. (1997). *Micro-optics: Elements, Systems and Applications,* Taylor & Francis, ISBN 0-7484-0481-3, London, England

Leith, E.N. & Upatnieks, J. (1962), Wavefront reconstruction and communication theory, *Journal of Optical Society of America* (October 1962), Vol. 52, Issue 10, pp. 1123-1128, ISSN 1520-8532

Levenson, M. D.; Viswanathan, N. S. & Simpson, R. A. (1982), Improving resolution in photolithography with a phase-shifting mask, *IEEE Transactions on Electron Devices* (December 1982), ED-29, Issue 12, pp. 1828-1836, ISSN 0018-9383

Levenson, M. D. (1993), Wavefront engineering for photolithography, *Physics Today* (July 1993) pp. 28-36, ISSN 0031-9228

Levenson, M. D. (1994), Extending the lifetime of optical lithography technologies with wavefront engineering, *Japanese Journal of Applied Physics* (September 1994), Vol. 33, pp. 6765-6773, ISSN 1347-4065

Levenson, M. D. (2006), Using destructive optical interference in semiconductor lithography, *Optics & Photonics News* (April 2006), pp. 30-35, ISSN 1047-6938

Lohmann, A. W. (1956), Optische Einseitenbandübertragung Angewandt auf das Gabor-Mikroskop," *Optica Acta* (June 1956), Vol. 3, pp. 97-100, ISSN 0030-3909

Lohmann, A.W. & Paris, D.P. (1967) Binary Fraunhofer holograms, generated by computer, *Applied Optics* (October 1967), Vol. 6, No.10, pp.1739-1748, ISSN 2155-3165

Lohmann, A. W. (2008). A Pre-History of Computer-Generated Holography, *Optics and Photonics News* (February 2008), pp. 36-41, ISSN 1047-6938

Mait, J. N. (1995) Understanding diffractive optic design in the scalar domain, Journal of Optical Society of America A (October 1995), Vol. 12, No. 10, pp. 2145-2158, ISSN 084-7529

Neto, L. G.; Roberto, L. B.; Mansano, R. D.; Verdonck, P.; Cirino, G. A. & Steffani (2001), M. A. Multiple Line Generation Over High Angle Using Hybrid Parabolic Profile and Binary Surface-Relief Phase Element, *Applied Optics* (January 2001), vol. 40, issue 2, pp.211-218, ISSN 2155-3165

Neto, L. G.; Cardona, P. S. P.; Cirino, G. A.; Mansano, R. D. & Verdonck, P. (2003) Design, fabrication, and characterization of a full complex-amplitude modulation diffractive optical element, *Journal of Microlithography, Microfabrication and Microsystems*, (April 2003), vol. 2, issue 2, pp. 96-104, ISSN 1537-1646

Neto, L. G.; Cardona, P. S. P.; Cirino, G. A.; Mansano, R. D. & Verdonck, P. (2004), Implementation of Fresnel full complex-amplitude digital holograms, *Optical Engineering*, (November 2004), vol. 43, No. 11, ISSN 0091-3286

Neto, L. G.; Mansano, R. D.; Cirino, G. A.; Zambom, L. S. & Verdonck, P. (2008), Amorphous hidrogenated carbon film (June 2008), *US Patent* 7,381,452

O'Shea, D. C.; Suleski, T. J.; Kathman, A. D. & Prather, D. W. (2004), *Diffractive Optics: Design, Fabrication, and Test*, Tutorial Texts in Optical Engineering Vol. TT62, SPIE Press, ISBN 0-8194-5171-1, Washington, USA

Seldowitz, M. A.; Allebach, J. P. & Sweeney, D. W., 1987, Sinthesis of digital holograms by direct binary search, *Applied Optics*, Vol. 26, No. 14, pp. 2788-2797, ISSN 2155-3165

Turunen, J.; Wyrowski, F. (1997). *Diffractive Optics for Industrial and Commercial Applications,* Akademie Verlag, ISBN 3-05-501733-1, Berlin, Germany

Wyrowski, F. (1989) Iterative quantization of digital amplitude holograms, *Applied Optics* (September 1989), Vol. 28, No. 18, pp. 3864-3870, ISSN 2155-3165

Wyrowski, F. (1990a) Diffractive optical elements: iterative calculation of quantized, blazed phase structures, *Journal of Optical Society of America A* (June 1990), vol. 7, pp. 961-969, ISSN 084-7529

Wyrowski, F. (1990b) Diffraction efficiency of analog and quantized digital amplitude holograms: analysis and manipulation, *Journal of Optical Society of America A* (March 1990), vol. 7, pp. 383-389, ISSN 084-7529

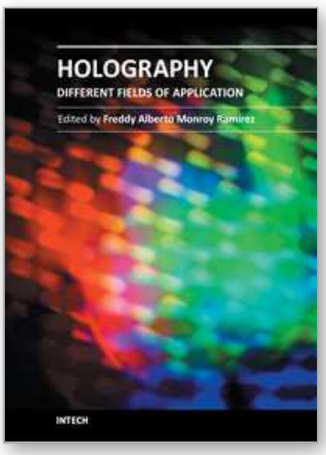

Holography - Different Fields of Application

Edited by Dr. Freddy Monroy

ISBN 978-953-307-635-5
Hard cover, 148 pages
Publisher InTech
Published online 12, September, 2011
Published in print edition September, 2011

This book depicts some differences from the typical scientific and technological literature on the theoretical study of holography and its applications. It offers topics that are not very commercial nor known, which will allow a different view of the field of optics. This is evident in chapters such as â€œElectron Holography of Magnetic Materialsâ€, â€œPolarization Holographic Gratings in Polymer Dispersed Formed Liquid Crystals, and â€œDigital Holography: Computer-generated Holograms and Diffractive Optics in Scalar Diffraction Domainâ€. The readers will gain a different view of the application areas of holography and the wide range of possible directions that can guide research in the fields of optics.

How to reference

In order to correctly reference this scholarly work, feel free to copy and paste the following:

Giuseppe A. Cirino, Patrick Verdonck, Ronaldo D. Mansano, José C. Pizolato Jr., Daniel B. Mazulquim and Luiz G. Neto (2011). Digital Holography: Computer-Generated Holograms and Diffractive Optics in Scalar Diffraction Domain, Holography - Different Fields of Application, Dr. Freddy Monroy (Ed.), ISBN: 978-953-307-635-5, InTech, Available from: http://www.intechopen.com/books/holography-different-fields-of-application/digital-holography-computer-generated-holograms-and-diffractive-optics-in-scalar-diffraction-domain

INTECH
open science | open minds

InTech Europe
University Campus STeP Ri
Slavka Krautzeka 83/A
51000 Rijeka, Croatia
Phone: +385 (51) 770 447
Fax: +385 (51) 686 166
www.intechopen.com

InTech China
Unit 405, Office Block, Hotel Equatorial Shanghai
No.65, Yan An Road (West), Shanghai, 200040, China
中国上海市延安西路65号上海国际贵都大饭店办公楼405单元
Phone: +86-21-62489820
Fax: +86-21-62489821

IntechOpen